Research Square

Preprints are preliminary reports that have not undergone peer review.
They should not be considered conclusive, used to inform clinical practice,
or referenced by the media as validated information.

Mapping Urban Flash Flood Damage Using High-Resolution Satellite Imagery

Mirela Tulbure

mtulbure@ncsu.edu

North Carolina State University https://orcid.org/0000-0003-1456-183X

Darcy Boast

North Carolina State University at Raleigh: North Carolina State University

Julio Caineta

North Carolina State University at Raleigh: North Carolina State University

Rebecca Composto

NC State University: North Carolina State University

Mollie Gaines

North Carolina State University at Raleigh: North Carolina State University

Research Article

Keywords:

Posted Date: November 20th, 2026

DOI: https://doi.org/10.21203/rs.3.rs-11039001/v1

License: This work is licensed under a Creative Commons Attribution 4.0 International License.
Read Full License

Mapping Urban Flash Flood Damage Using High-Resolution Satellite Imagery

Mirela G. Tulbure[12*], Darcy Boast[1], Júlio Caineta[2], Rebecca Composto[1], Mollie D. Gaines[2]

[1] Center for Geospatial Analytics, North Carolina State University, Raleigh, USA
[2] Department of Forestry and Environmental Resources
[*] Corresponding author: mtulbure@ncsu.edu

Abstract: Mapping flood damage in urban areas is challenging due to factors including building density and flash floods exacerbated by impervious surfaces. Often called "Appalachia's Katrina", Hurricane Helene was the deadliest mainland US storm since Hurricane Katrina, with more than 200 deaths and an estimated $78.7 billion in damage. In this study, we used PlanetScope high-spatial- and temporal-resolution satellite data and machine learning to, for the first time, map flood extent across heavily impacted counties in western North Carolina, focusing on Asheville, the region's largest city and previously deemed a "climate haven". Random forest classification of pre-, peak-, and post-flood imagery achieved high accuracy (98.8–99.9% overall accuracy), though extensive cloud cover limited peak-flood classification, and models struggled to detect narrow waterways. To assess damage, we combined the flood extent maps with the Federal Emergency Management Agency (FEMA) flood zones, FEMA USA Structures, and Black Marble nighttime lights data. Comparison with FEMA's 100-year flood zone in Asheville showed 94.76% overall pixel-level agreement, though only 40.57% agreement among pixels flooded by at least one layer, with more flooding missed within the FEMA zone (4.24% of pixels) than mapped outside it (1.01%). We identified 272 buildings intersecting the mapped flood extent in Asheville, though this likely underestimates total structural damage. Nighttime-lights anomalies were most severe in Asheville and surrounding western counties, consistent with the scale of reported damage there. These findings quantify flood extent and damage across western North Carolina and show how high-resolution satellite imagery can support emergency preparedness and response, while also highlighting key limitations, such as cloud cover, that constrain rapid post-storm imagery-based assessment.

Key words: PlanetScope, Machine learning, Hurricane Helene, flash floods, urban floods

1. Introduction

Floods are among the most common and most dangerous weather-related hazards, with some of the highest costs to human life, infrastructure, and economic recovery (Chen et al., 2020; World Meteorological Organization (WMO), 2023). Flood events can cause both immediate danger and lasting damage. Certain areas are at high risk of flash flooding, including urban areas, riverbanks, and mountainous regions (NOAA National Severe Storms Laboratory, 2024). Flash flooding is especially deadly and occurs quickly after heavy rainfall (Xia et al., 2011). During flash floods, water rises quickly, giving people little time to reach safety. Fast-moving floodwaters increase the risk of drowning. Even after floodwaters recede, residents face an increased risk of disease from water contaminated with sewage and other contaminants (Coulson, 2024). As climate change warms the atmosphere, more intense and frequent

precipitation events are expected to cause more flood events (Anderson et al., 2022; Balaguru et al., 2023; Salarieh et al., 2023).

Floods cause extensive structural damage to homes, businesses, and infrastructure, including roads and power lines. In the U.S., the total cost of flooding is estimated to be $179.8 to $496 billion per year (United States Congress Joint Economic Committee, Democratic Staff, 2024). This risk is growing because many densely populated urban areas are along coasts and waterways, and populations in these flood-prone areas are projected to continue increasing over the next 25 years (Aerts et al., 2014). Growing populations increase impervious surface area (i.e., developed land cover such as paved roads and parking lots), which limits natural drainage and increases runoff, even from mild rainfall (Aziz et al., 2024). Urban areas often have some form of built flood defense (e.g., dams or stormwater retention ponds), which can decrease initial flood risk but can also lead to more disastrous flooding if they fail (Armon et al., 2025; Aziz et al., 2024). Information on flood extent and damage is critical to aid recovery efforts after flooding. Earth Observation (EO) data offer one of the few ways to derive such flood information consistently across space and time and have successfully been used to map surface water and flood extent (Composto et al., 2024; Tulbure et al., 2022, 2016).

EO data have been used to map flood events, but mapping floods in urban areas is particularly challenging. Most flood maps have been derived from public, optical EO data, such as Landsat and Sentinel-2 (Munawar et al., 2022; Tulbure et al., 2022), but these data have a number of limitations, including coarse spatial resolution, long return time, and cloud obstruction (Langhorst et al., 2024; Tulbure et al., 2022). These limitations are especially problematic for urban flash floods, which can last less than a day: mapping such events requires a short satellite revisit time—24 hours or up to 3 days—to acquire imagery within the timeframe emergency response agencies need (Hodgson et al., 2009). Coarse spatial resolution further limits the ability to capture the fine-grained detail of complex urban landscapes, and dense buildings can cause occlusion (Tan et al., 2024). Cloud coverage limits data availability before, during, and after flood events, and building shadows can interfere with the spectral signature of urban surfaces, causing them to appear flooded when they are not.

To address spatial and temporal resolution limitations of EO imagery, studies increasingly use commercial data (i.e., PlanetScope, WorldView, Capella) to map and assess flood dynamics (Jensen et al., 2022; Shastry et al., 2023). Given the near-daily revisit frequency, high spatial resolution, and data volume, commercial EO data are more likely to capture ephemeral flood events than publicly available EO data (Tulbure *et al.*, 2022). For example, despite some limitations pertaining to spectral resolution, geolocation inaccuracies, and inconsistent radiometric calibration across multiple platforms, the suitability of PlanetScope and WorldView data has been shown in hydrology applications, including surface water and flood mapping (Hondula et al., 2021; McCabe et al., 2017; Mullen et al., 2023; Shastry et al., 2023). PlanetScope's high spatial (3 m) and temporal (near-daily) resolution makes it particularly well suited to flood extent mapping.

While tropical cyclones, including hurricanes, tropical storms/depressions, and typhoons, bring hazards ranging from strong winds to storm surge, flooding is the main danger to both coastal and inland communities (Rappaport, 2014; Zhang et al., 2018). Although the number of recorded floods caused by tropical cyclones is relatively small compared with the total number of flood events over time, their impact (e.g., fatalities or displaced people) is disproportionately high. Most inland flooding from tropical cyclones results from extreme precipitation (Noh et al., 2019; Zhu and Quiring, 2022). Since the 1940s, the average translational speed of tropical cyclones along the North American coast has slowed by about 17% (Hall and Kossin, 2019). These slower tropical cyclones have increasingly stalled inland and increased precipitation (Hall and Kossin, 2019). Extreme precipitation is predicted to increase by at least 6–7% for each 1 °C of local temperature warming due to increased saturation specific humidity (Risser and Wehner, 2017). Per 1 °C of human-driven global warming, a 25–30% global increase in severe hurricanes (category 4–5) has been observed (Holland and Bruyère, 2014). Tropical cyclone precipitation is predicted to increase due to both an increase in rainfall from climate warming and more frequent stalling due to a decrease in translational speed (Hall and Kossin, 2019; Knutson et al., 2020; Patricola and Wehner, 2018).

Hurricane Helene made landfall near Perry, Florida, as a Category 4 hurricane (wind speeds 130–156 mph) late on September 26, 2024, then weakened to a tropical storm and moved into western North Carolina (WNC) (Callaghan, 2025). NOAA's National Centers for Environmental Information estimated $78.7 billion in damage nationwide, making Helene the seventh-costliest U.S. hurricane on record (adjusted to 2024 values) (Hagen et al., 2026). In North Carolina alone, damage is estimated at $59.6 billion (Cooper, 2024). Rainfall was extreme and prolonged: over a four-day period from September 25–28, WNC received what is typically several months' worth of rainfall, with a peak 3-day total of ~80 cm in Yancey County (Hagen et al., 2026), on top of ground already saturated from prior rain that week. Although Helene's rainfall and flooding were extreme, WNC has a documented history of severe flooding from tropical cyclones, including three storms in 2004 alone and record flooding in 1916 (Amorim et al., 2025), suggesting the region's vulnerability to tropical cyclone-driven flooding had historical precedent, even if severe. The flooding and landslides caused catastrophic damage across Asheville, Boone, Swannanoa, Chimney Rock, Banner Elk, and other mountain communities, disrupting timberland, roads, bridges, homes, and access to water and power for weeks (Hagen *et al.*, 2026). The area around Asheville alone accounted for 157 of the 250 total fatalities recorded across the United States (Callaghan, 2025). The U.S. Coast Guard rescued more than 850 people from floodwaters in WNC (Callaghan, 2025).

Several studies have examined Hurricane Helene's impacts in WNC using flood exposure data derived from satellite and terrain-based methods, including a SAR-based inundation product combined with social vulnerability indicators (First et al., 2026) and a terrain-based (height above nearest drainage) flood mapping approach compared against FEMA's 100-year flood zone (Pieper et al., 2025). However, to our knowledge, no study has derived a high-resolution, optical satellite-based flood extent map for the region, and no study has fully assessed building- and infrastructure-level damage using satellite imagery. Therefore, the goals of this study are to 1) calculate flood extent before, during, and after Hurricane Helene in WNC, 2) calculate

percent flooded area per zip code tabulation area (ZCTA) and county, 3) compare flood maps to the FEMA 100-year flood hazard area (i.e., areas with a 1% annual chance of flooding), 4) intersect the FEMA USA Structures dataset with our calculated flood extent, and 5) assess damage by comparing nighttime lights before and after the storm.

2. Methods

2.1 Study area. In this study, we focus on six counties in WNC (Ashe, Watauga, Mitchell, Yancey, Avery, and Buncombe) and Asheville in Buncombe County for FEMA flood-risk zone comparisons and intersection with the FEMA USA Buildings dataset. We selected these six counties because they sustained the most severe flood damage from Helene in WNC, and we selected Asheville for the flood-zone and structures analyses because it is the largest population center in the study area and experienced substantial, well-documented flood damage to both infrastructure and housing (Hagen et al., 2026). The city is located at the intersection of two major rivers, the French Broad and Swannanoa. Hurricane Helene caused historic flooding and damage to Asheville's lower-lying areas along both rivers (Hagen et al., 2026): the French Broad River crested at 7.52 m and the Swannanoa River at 8.0 m, both exceeding the previous all-time records set during the 1916 flood (Callaghan, 2025). Hurricane Helene also damaged Asheville's water treatment infrastructure, which took 53 days to repair, and the power grid, leaving 25,000 customers without power for two weeks (Hagen et al., 2026). We focused on Asheville because of the significant damage it sustained and its unique status as a "climate haven" (Simon, 2024).

A "climate haven" is an area perceived to be protected from global warming or where the effects of climate change can be managed (Khan et al., 2025). Asheville is perceived as a climate haven because of its inland mountain location between the Blue Ridge Mountains and the Great Smoky Mountains, which is scenic and keeps summers mild. From 2020 to 2024, the city's population grew by over 3,500, and it is the largest city in WNC, with a population of ~100,000 (Cline, 2024).

2.2 Satellite imagery selection. To quantify flood extent and impact, we looked for satellite imagery that overlapped with Hurricane Helene's flooding footprint, including Sentinel-2, Landsat 8 and 9, and NOAA aerial imagery. No Sentinel-2, Landsat 8, or Landsat 9 imagery was available in WNC during peak flooding. NOAA aerial damage assessment imagery was collected 5-6 days after Helene passed through Asheville and did not capture flooding (National Geodetic Survey, 2024). We used commercial optical imagery because it overlapped with peak flooding. However, cloud cover obscured most of WNC. We further focused on Asheville's downtown because the River Arts District was heavily damaged (Hagen et al., 2026) and satellite imagery captured the peak of the flood.

We chose PS imagery because of its near-daily temporal resolution and high spatial resolution (3 m) (Planet Labs, 2026), and because other imagery sources did not overlap with the flood event in our study area. We used a free educational account to access PS imagery (https://www.planet.com/industries/education-and-research/) and downloaded the data directly from the Planet Insights Platform. We used PS imagery collected pre-flood (September 20,

2024), peak-flood (September 28, 2024), and post-flood (October 5, 2024) for our study area. The pre- and post-flood images had minimal cloud cover, and the peak-flood images had 75-78% cloud cover. A cloud gap in the day-of-flood image made the River Arts District, which sustained heavy flooding and damage, visible. For all images, we used Planet's usable data mask (UDM2) to mask out clouds, haze, and other unusable pixels and kept only clear pixels (Perin et al., 2022). We mosaicked the image tiles into pre-, peak-, and post-flood images using QGIS.

2.3 Random forest. The Random Forest (RF) classifier is a machine learning algorithm effective for classifying pixels in satellite imagery (Maxwell et al., 2018). The RF classifier uses many decision trees, each trained on a random subset of data and input features, and then takes a majority vote across all trees to classify the data (Breiman, 2001). We selected the RF classifier because it has a low computational cost compared to deep learning models and is robust to small training datasets (Maxwell et al., 2018). We also selected the RF classifier because of its high accuracy in classifying both surface water (Gaines et al., 2024; Hondula et al., 2021; Phan et al., 2020) and flooding (Tulbure *et al.*, 2022; Composto *et al.*, 2024).

We used seven input features for the RF models, including the four spectral PS bands (red, green, blue, near-infrared). We also included three derived indices, including the Normalized Difference Water Index (NDWI) (McFeeters, 1996), Normalized Difference Vegetation Index (NDVI) (Kriegler et al., 1969), and Normalized Impervious Surface Index (NISI) (Su et al., 2022).

We drew water and non-water polygons in QGIS using PS imagery for the study dates and study area of Asheville, NC. We created three training and testing datasets for three separate models: pre-flood, peak-flood, and post-flood. The pre-flood dataset included 47 water polygons (15,888 pixels) and 10 non-water polygons (18,857 pixels). The peak-flood dataset had 22 water polygons (8,817 pixels) and 23 non-water polygons (253,386 pixels). The post-flood dataset had 46 water polygons (15,614 pixels) and 6 non-water polygons (15,788 pixels).

We ran the RF algorithm in VS Code using Python's Scikit-learn library (Pedregosa et al., 2011). We used the *train_test_split* function to split the data into 85% training and 15% testing. We applied the *RandomForestClassifier* function to train the model on the training dataset. To assess accuracy, we used the testing data to create a confusion matrix and computed overall accuracy, precision, recall, and F1-Score (Landwehr et al., 2024). We applied the trained model to the imagery, producing pre-, peak-, and post-flood maps for each day.

2.4 USA Structures Dataset. After classifying flood and water extent (as in Section 2.3 above), we used zonal statistics to identify how many structures from the FEMA USA structures dataset overlapped the flood extent during peak flood on September 28, 2024. The FEMA USA structures dataset is a publicly available inventory of structures in the U.S. that are larger than ~42 m^2 (FEMA, 2026). Outlines were extracted from satellite imagery, along with occupancy type (e.g., residential, commercial, or industrial). In addition to occupancy, the attributes include primary occupancy (subset categories), a universal unique identifier (UUID), address, city, state, zip, and square footage.

2.5 Percent Water ZCTA and County Comparisons. ZIP Code Tabulation Areas (ZCTAs) are polygons the U.S. Census Bureau created to represent areas containing point-based ZIP code features (U.S. Census Bureau, 2020). We calculated the percent water pre-, peak-, and post-flood at the ZCTA and county level. We calculated the percentage of water pixels by dividing the number of water pixels by the total number of valid pixels per polygon (i.e, ZCTA, county). We defined valid pixels as cloud-free pixels. We also calculated the percent invalid pixels (i.e., cloudy) per polygon. Percent water area was calculated by dividing the area of water (the number of water pixels times the area of one pixel, 9 m^2) by the total area of the polygon.

2.6 NTL damage assessment. Nighttime lights (NTL) can be captured via remote sensing and represent artificial nocturnal light generated by human activities (Xu and Qiang, 2021). NTL is used in many types of research, including studying shipping vessels and aerosols and monitoring human activity, such as estimating poverty (Shao and Li, 2023a; Wang, 2022). NTL is also used after disasters to assess changes in human activity intensity (Zheng et al., 2025) and to detect property damage, power outages, and economic recovery (Xu and Qiang, 2021).

The National Aeronautics and Space Administration (NASA) Black Marble product suite (VNP46/VJ146) is a global nighttime lights product with a spatial resolution of 15 arc-seconds (about 500 m) and at daily, monthly, and yearly time steps from 2012 to the present. NASA developed this product suite using the Day/Night band (DNB) of the Visible Infrared Imaging Radiometer Suite (VIIRS) (Wang, 2022). The Black Marble product is moonlight-adjusted and measures radiance (nWatts·cm^{-2}·sr^{-1}) (Wang, 2022).

We used two products for our NTL analysis: the VNP46A2 daily product and the VNP46A3 monthly product. We downloaded the VNP46A3 monthly product for August 2024 (one month before the storm) and the VNP46A2 daily product for October 10, 2024 (one day post-storm) using the *BlackMarblePy* Python package developed by the World Bank (Vicente and Marty, 2024). For each product, we selected the “AllAngle_Composite_Snow_Free” data, which is a temporal radiance composite using all observations during the snow-free period (Wang, 2022). We selected the all-angle composite (near-nadir, off-nadir, and all angles) because the multi-angle product provides more ground information (Shao and Li, 2023b) and is snow-free. We then filtered out the fill value of 65500 and multiplied the data by 0.01 (Wang, 2022). We also filtered out very small values (0.1) to reduce noise in dark areas.

We calculated the change in NTL by computing the pixel-wise standard anomaly between one month before the storm (August 2024) and one day after the storm (October 10, 2024) in QGIS. For each county in the study area, we calculated the mean and sum of the resulting values. We divided each county's sum by its area.

3. Results

3.1 Flood extent from RF model

We created a new flood extent for the study area during peak flood on September 28, 2024. We also created a pre-flood water extent for September 20, 2024, and a post-flood water extent for October 5, 2024 (Fig. 1). Each extent has two classes: water and non-water. We assessed accuracy using the reserved test data and generated confusion matrices (Table 1). We calculated overall accuracy, precision, recall, and F1-Score for each of the three models.

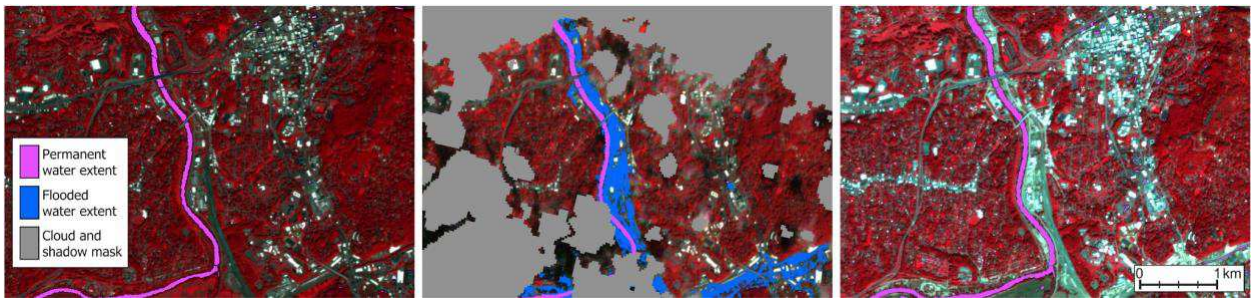


Fig. 1 *RF-derived surface water extent over 3-m PlanetScope imagery for Asheville, NC, before Hurricane Helene (left; September 20, 2024), during peak flood (middle; September 28, 2024), and one week after the event (right; October 5, 2024); imagery is shown as a false-color composite (R: NIR, G: red, B: green), with clouds and cloud shadows masked in gray. Water mapped in the pre-flood image was treated as permanent water and shown in magenta; flood water mapped in the peak- and post-flood images is shown in blue, with the pre-flood extent overlaid for reference.*

Overall classification accuracy was high across the three acquisition dates, although the peak-flood model showed lower recall and F1-score, likely due to cloud coverage (Table 1).

Table 1. Overall accuracy and class-specific precision, recall, and F1-score for the pre-flood, peak-flood, and post-flood surface water extent models.

Model	Class	Overall accuracy (%)	Precision (%)	Recall (%)	F1-score (%)
Pre-flood	Water	98.79	99.28	**98.07**	98.67
	Non-water		98.39	99.40	98.89
Peak-flood	Water	99.57	96.85	**89.78**	93.18
	Non-water		99.65	99.90	99.78
Post-flood	Water	99.94	100.00	**99.87**	99.94
	Non-water		99.87	100.00	99.94

3.2 Percent flooded area per ZCTA and county

The ZCTA- and county-level analyses show the spatial distribution of aggregated surface water across the study area. From pre-flood to peak-flood, 33 of the 66 ZCTAs with valid observations (50.0%) shifted to a higher percent-water-pixel class, including several ZCTAs around Asheville and Hendersonville; 28 remained in the same class, and 5 shifted to a lower class, while 20 ZCTAs had no data at peak flood (Figure 2). From pre-flood to post-flood, 26 of 86 ZCTAs (30.2%) shifted to a higher percent-water-pixel class, 59 remained in the same class, and only one shifted to a lower class, suggesting that some floodwater may have remained one week after the event. In contrast, 60 of the 66 ZCTAs with valid observations (90.9%) had less than 1.5% mapped water area at peak flood, including 49 (74.2%) in the lowest class (less than 0.5%). Extensive cloud and cloud-shadow contamination in the peak-flood image likely explains this difference: the percent water area metric uses the full polygon area as the denominator, including areas represented by invalid pixels, which reduces the apparent proportion of mapped water where valid observations are limited.

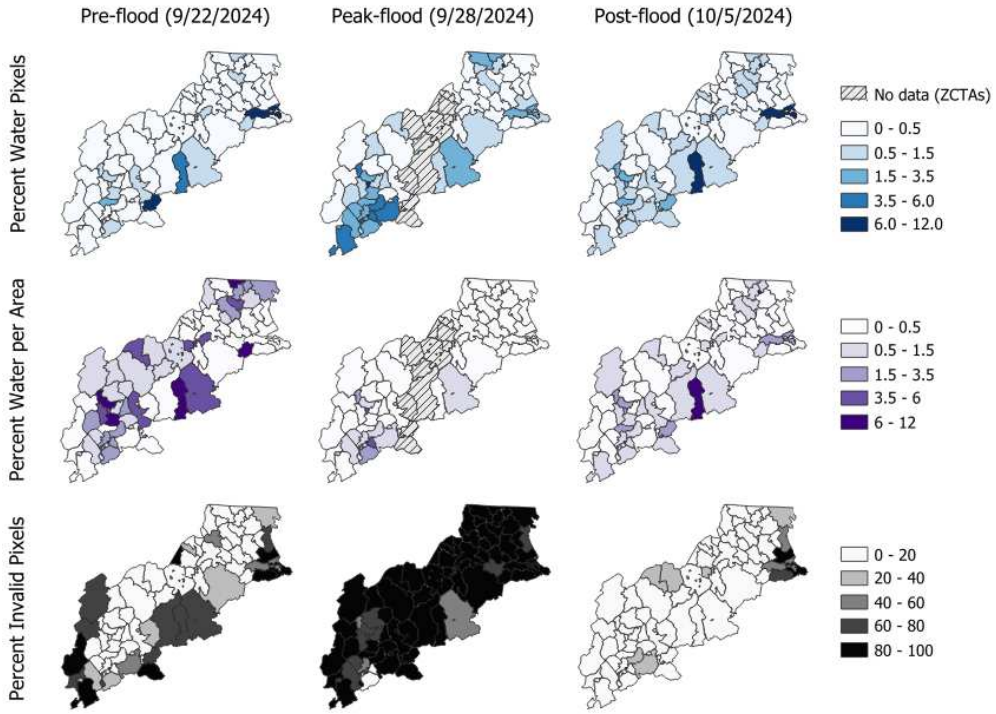


Fig. 2 *Percent water pixels, percent water area, and percent invalid pixels by ZIP Code Tabulation Area (ZCTA) for pre-flood (September 22, 2024), peak-flood (September 28, 2024), and post-flood (October 5, 2024) conditions. Percent water pixels is calculated relative to valid pixels within each polygon, whereas percent water area is calculated relative to the full polygon area.*

The county-level aggregation showed a similar pattern (Figure 3). From pre-flood to peak-flood conditions, 9 of the 16 counties with valid observations (56.3%) shifted to a higher percent-water-pixel class, while 5 remained in the same class and 2 shifted to a lower class. By the post-flood date, 15 of 18 counties (83.3%) were in a higher percent-water-pixel class than before the event, indicating that mapped surface water remained elevated across much of the

study area. In contrast, 14 of the 16 counties with valid observations (87.5%) had less than 0.3% mapped water area at peak flood. This low value reflects the extensive invalid coverage in the peak-flood image: 15 of 18 counties (83.3%) had 80–100% invalid pixels, and all counties had more than 60% invalid coverage.

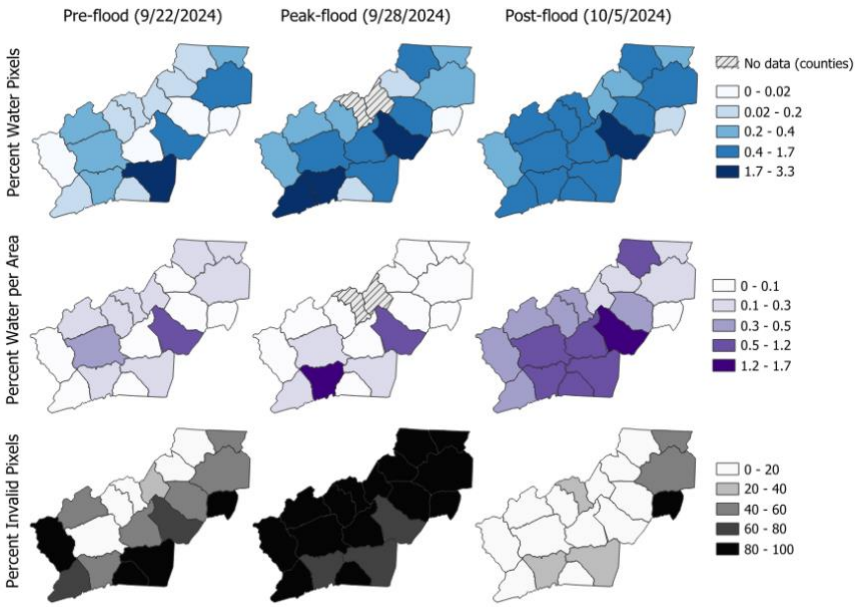


Fig. 3 *Percent water pixels, percent water area, and percent invalid pixels by county for pre-flood (September 22, 2024), peak-flood (September 28, 2024), and post-flood (October 5, 2024) conditions.*

3.3 Flood extent comparison to FEMA flood risk zones

In Asheville, the derived Helene flood extent and the FEMA 100-year flood zone showed 94.76% overall pixel-level agreement (Figure 4). However, this high agreement was largely driven by pixels classified as non-flooded in both layers. Among pixels identified as flooded by at least one layer, 40.57% were flooded in both. Of all pixels, 1.01% were mapped as flooded during Helene but fell outside the FEMA 100-year flood zone, while 4.24% fell within the FEMA 100-year flood zone but were missing from our flood extent.

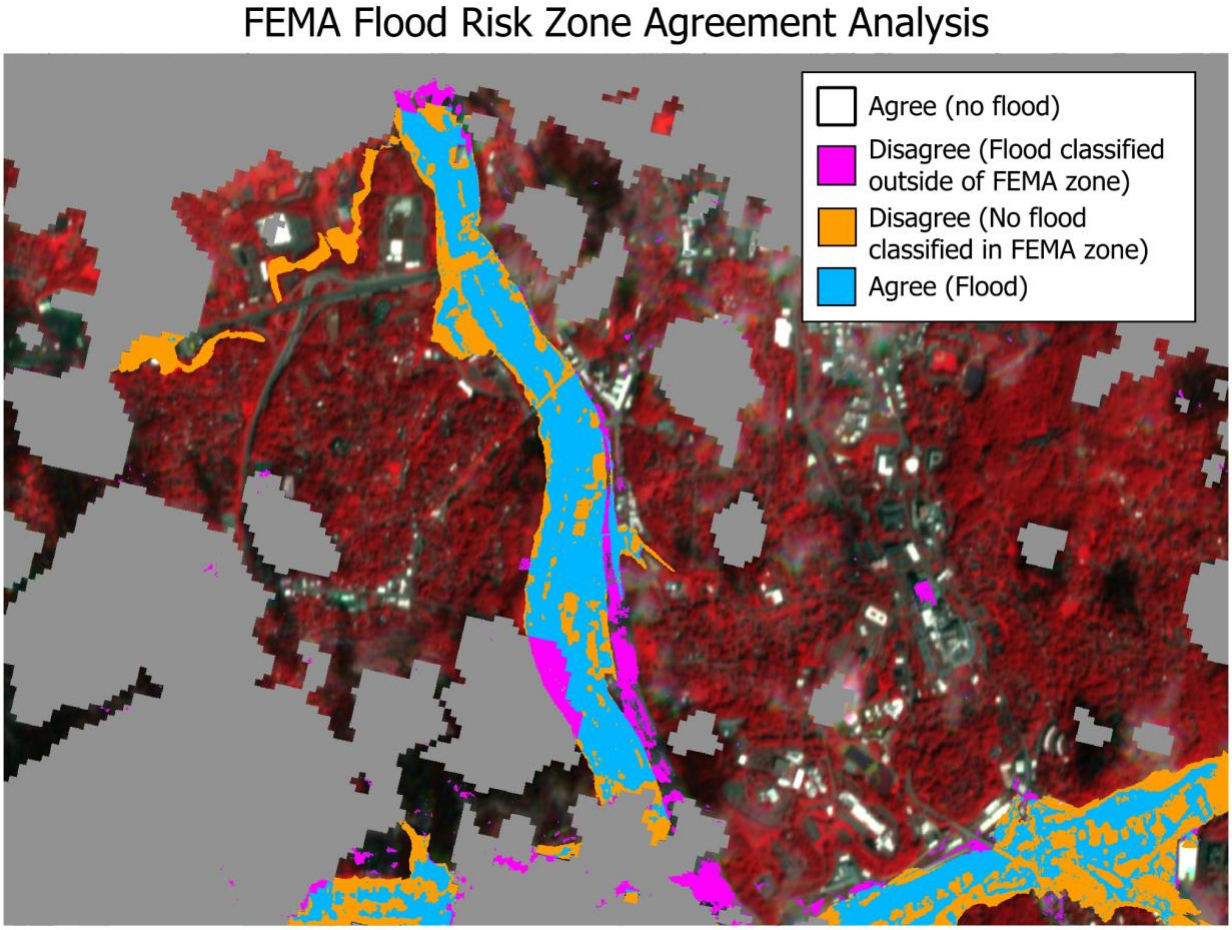


Fig. 4 *Pixel-level agreement between the FEMA 100-year flood zone and the mapped Hurricane Helene flood extent in Asheville, NC, over 3-m PlanetScope imagery. Colors indicate agreement for flooded (blue) and non-flooded pixels and disagreement where mapped flooding occurred outside the FEMA zone (magenta) or where FEMA-zone pixels were not classified as flooded (orange). PlanetScope imagery is shown as a false-color composite (R: NIR, G: red, B: green), with masked clouds and shadows shown in grey (PS UDM2), also highlighting missed cloud shadows and haze.*

3.4 Flood extent intersection with FEMA USA structures dataset

The intersection of our flood extent with building footprints (FEMA USA Structures) in Asheville illustrates how satellite imagery-derived flood mapping supports rapid impact assessment. Using zonal statistics, we identified 272 building footprints intersecting the mapped flood extent during peak flood on September 28, 2024, and flagged them as affected. The resulting affected buildings spatially coincided with areas of visible inundation in the PS imagery (Figure 5). As expected, this count likely underestimates total structural damage, since damage mechanisms such as flooded basements or wind damage are not visible from satellite imagery.

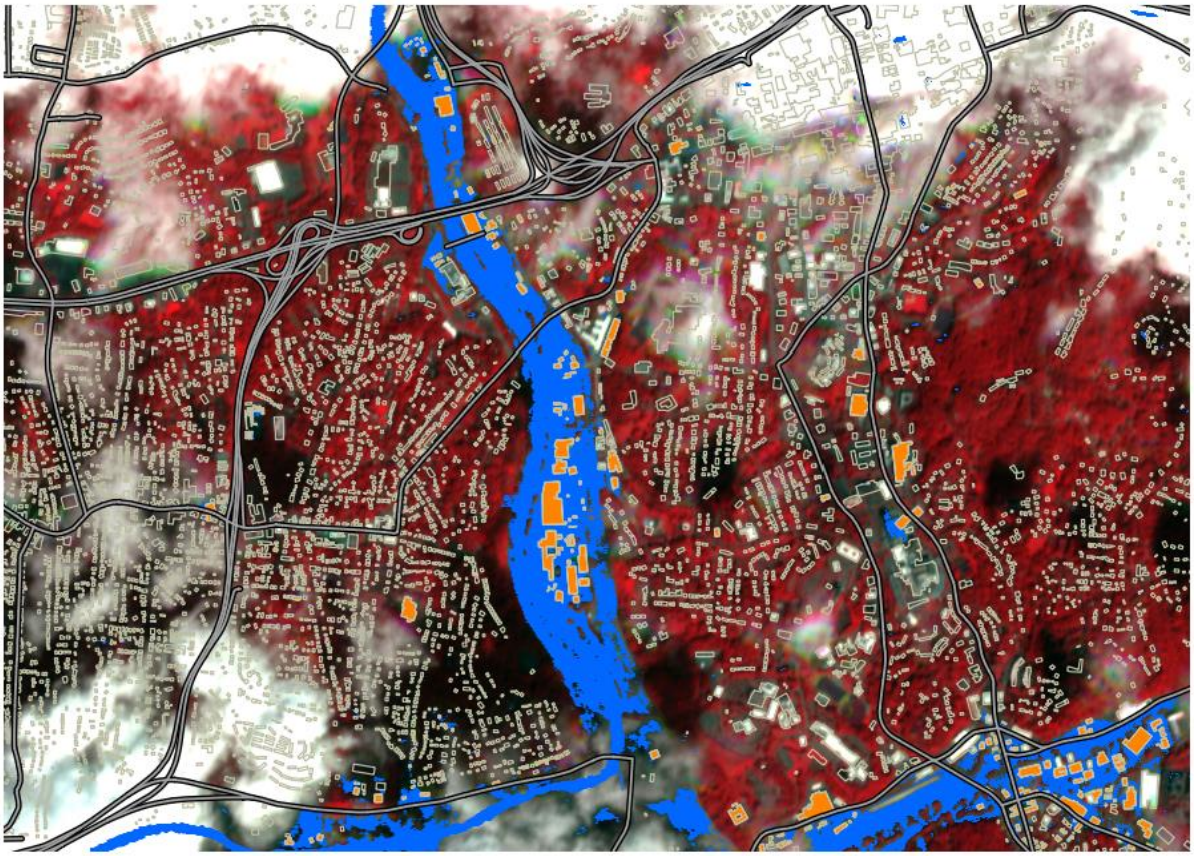


Fig. 5 *Building footprints intersecting the mapped Hurricane Helene flood extent in Asheville, NC, over 3-m PlanetScope imagery. Blue indicates mapped surface water, and orange indicates FEMA USA Structures building footprints that intersect the flood extent. PlanetScope imagery is shown as a false-color composite (R: NIR, G: red, B: green).*

3.5 Nighttime lights damage assessment

We calculated two nighttime-lights change metrics: the mean standardized anomaly, which represents damage severity, and the area-normalized standardized anomaly sum, which represents how much of each ZCTA or county was affected. The ZCTAs surrounding Asheville scored highest for both metrics (Figure 6). At the county level, Buncombe County—where Asheville is—also scored highest for both metrics (Figure 7).

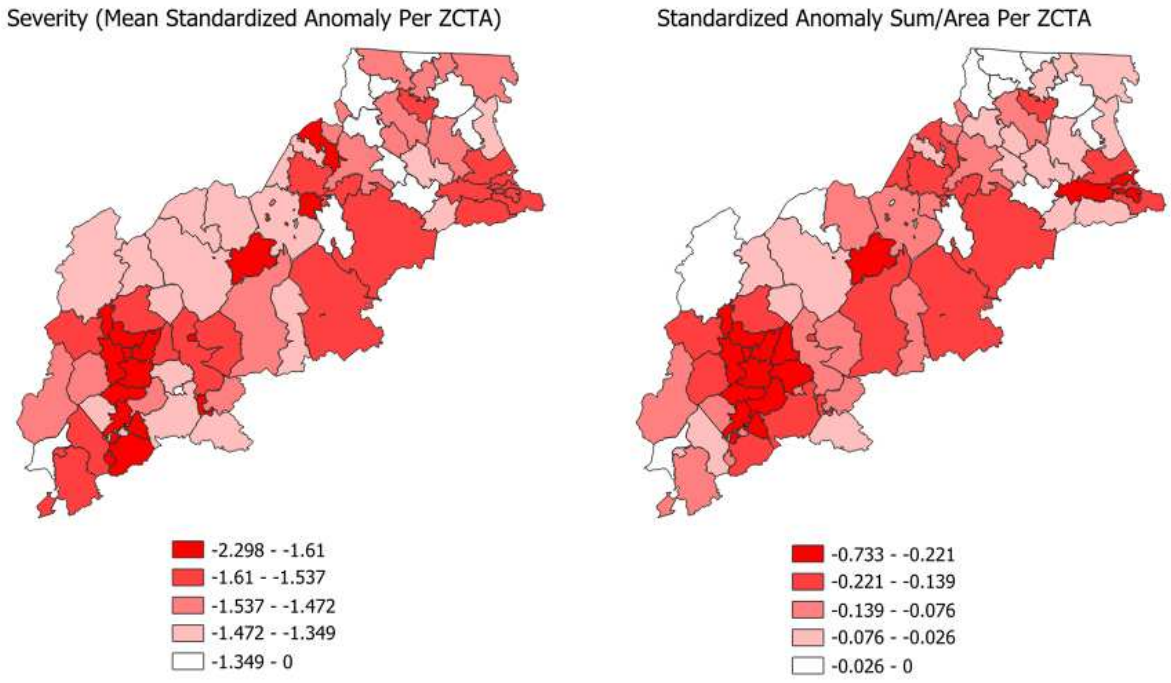


Fig. 6 *ZCTA-level nighttime-lights change following Hurricane Helene, shown as mean standardized anomaly (left) and area-normalized standardized anomaly sum (right). Larger negative values indicate greater reductions in nighttime lights.*

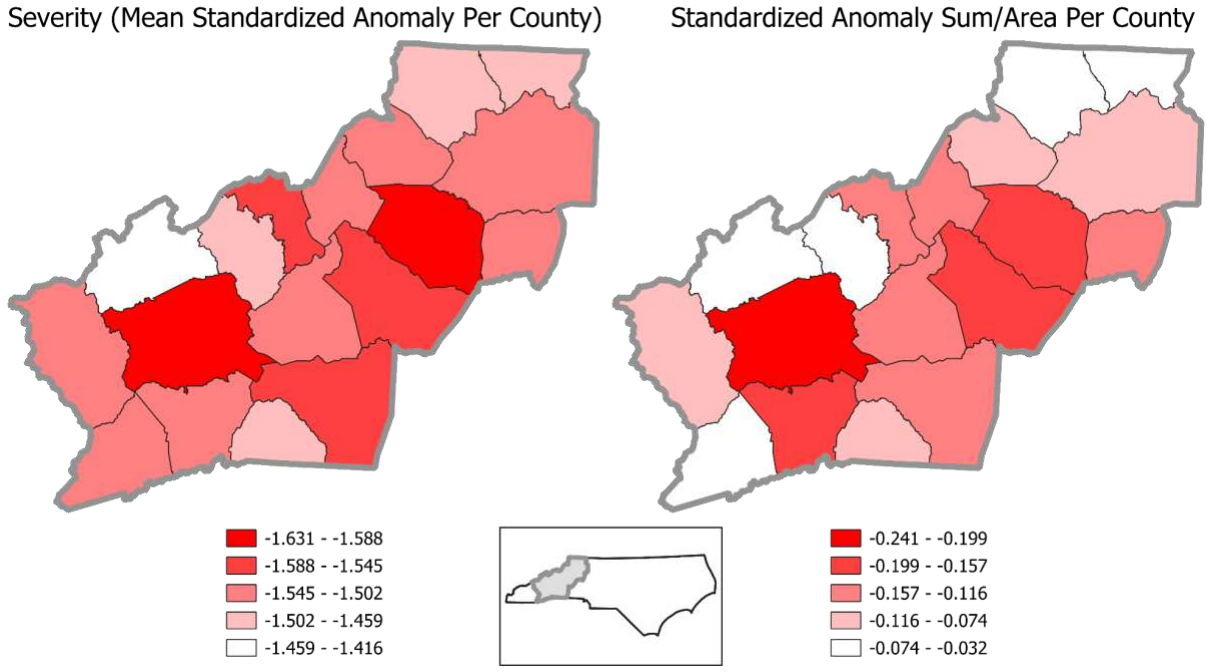


Fig. 7 *County-level nighttime-lights change following Hurricane Helene, shown as mean standardized anomaly (left) and area-normalized standardized anomaly sum (right). Larger negative values indicate greater reductions in nighttime lights. The inset shows the study area's location within North Carolina.*

4. Discussion

This study demonstrates the effectiveness of high-resolution optical satellite imagery (PS) and machine learning for mapping flood extent and assessing damage in a complex, mountainous urban environment. Using PS imagery and an RF classifier, we generated pre-, peak-, and post-flood water extent maps for WNC during Hurricane Helene, achieving relatively high classification accuracy despite substantial cloud cover, haze, and urban complexity (Table 1). This performance compares favorably with prior studies that have used PS data to map event-specific floods. For example, prior research (Pastor-Escuredo et al., 2020) estimated flood areas by digitizing and subtracting areas visually interpreted as floods from pre- and post-flood imagery. Others (Wang and Vivoni, 2022) used PS data during a fatal flood event (13–14 August 2021) in Gila Bend, Arizona, applying a similar pre/post-flood approach based on the difference in NIR reflectance (NIRFlood − NIRDry), with dNIR ≤ 0.5 representing ponded water and > 0.02 representing flood-affected areas. Similarly, prior research (Levin and Phinn, 2022) mapped flooding in Brisbane during the 2022 Australian summer floods using pre- and peak-flood PS imagery and a Normalized Difference Inundation Index (NDII), calculated as the difference in NIR reflectance between pre- and peak-flood dates. The threshold used to derive flooded areas (0.1) was visually chosen based on the NDII histogram. Unlike these manually thresholded approaches, our RF classifier offers a data-driven alternative that can generalize across areas without requiring a new visually derived threshold for each event.

Despite challenges such as cloud cover, haze, and urban complexity, our flood models achieved relatively high accuracy (Table 1), consistent with other studies applying RF classification to PS imagery for flood mapping (Composto et al., 2024). We used Planet's UDM2 layer to mask clouds, cloud shadow, and haze before classification, but the mask was imperfect: some haze and cloud shadow remained in the imagery, particularly in the peak-flood scene. This is reflected in the peak-flood model's lower recall relative to the pre- and post-flood dates (Table 1), as residual haze and shadow likely caused some flooded pixels to be misclassified as non-water.

Although overall accuracy was high, the models also struggled to detect narrow rivers and streams. Ross Creek, which runs north-south along the eastern side of the study area (Figure 1), was not captured by any of our three models, likely due to its narrow width relative to the 3-m pixel resolution. Wider rivers were also detected inconsistently across dates: the Swannanoa River (visible in the bottom right of Figure 1) was captured as flooded in the post-flood scene but was missing from the pre-flood classification, even though the river channel should have been present at both dates. This suggests our models were more sensitive to detecting rivers when floodwaters widened them beyond their normal channel width, and were less reliable at capturing narrower waterways under typical, non-flood conditions.

By combining multiple data sources, we gained a more comprehensive understanding of Hurricane Helene's impacts. The ZCTA- and county-level percent-flooded analyses (Figures 2 and 3) show that mapped surface water increased broadly across the study area from pre-flood

to peak-flood, remained elevated one week later, and that flood damage was most severe around Asheville and southwestern ZCTAs (Figure 2) and counties (Figure 3). Half of ZCTAs with valid data shifted to a higher percent-water-pixel class by peak flood, and the majority remained elevated at the post-flood date, suggesting some floodwater had not yet fully receded a week after the storm. This pattern was consistent at the county level, where 15 of 18 counties remained in a higher water-pixel class by the post-flood date than before the storm.

In contrast, the percent-water-area metric showed a markedly different, and considerably lower, pattern at peak flood: most ZCTAs and counties had less than 1.5% and 0.3% mapped water area, respectively, during peak flooding. This divergence between the two metrics is a data-completeness artifact, not evidence of limited flooding. Because percent water area is calculated relative to each polygon's full area, it is directly suppressed by the extensive cloud and cloud-shadow contamination present in the peak-flood imagery (Figure 1), with all counties having more than 60% invalid pixel coverage at peak flood, and most having 80–100% invalid coverage. Percent water pixels, calculated only relative to valid (cloud-free) pixels, better reflects flooding intensity where imagery was usable, but does not indicate how much of a given polygon that assessment covers. Together, these two metrics illustrate a key constraint of optical flood mapping during active storm events: the areas most likely to be heavily flooded are often also the areas most obscured by cloud cover during peak flooding, meaning peak-flood water extent should be interpreted as a lower bound constrained by data availability, not a complete picture of flood severity across the study area.

In Asheville, our comparison to FEMA's 100-year flood zone revealed disagreement in both directions. The larger share of disagreement was flooding that FEMA's 100-year zone predicted, but our extent did not capture: 4.24% of all pixels fell within the FEMA 100-year zone but were not classified as flooded in our extent, likely reflecting residual, unmasked cloud shadow and haze in exactly these areas (Figure 4) rather than a genuine absence of flooding. However, 1.01% of all pixels were mapped as flooded outside the FEMA 100-year zone, a smaller share, but still meaningful evidence that flooding was not confined to FEMA's highest-risk designation. This finding is consistent with a broader body of work showing that flooding and associated damage regularly occur outside the FEMA 100-year flood zone (Collins et al., 2022) and that FEMA flood zones can underestimate flood exposure more broadly (Wing et al., 2018). This pattern of substantial local variability despite broad regional alignment is consistent with prior research (Pieper et al., 2025), which compared a terrain-based flood mapping approach (height above the nearest drainage) to FEMA's 100-year zone across 25 disaster-declared WNC counties and found close overall agreement (median ratio of estimated-to-FEMA flooded area of 1.05) but substantial county-level differences, reflecting that flood severity varied considerably across the region during Helene.

Our comparison was limited to the 100-year zone alone. Composto et al. (2024), using a similar PS-based RF approach to map flooding from Hurricane Ida in the Philadelphia metropolitan area, compared satellite-derived flood extent against the full range of FEMA zones and found that, across all counties studied, more flooding by area and percent occurred in FEMA's Minimal Hazard zone than in the 500-year zone, reinforcing the concern that areas classified as minimal risk are not, in practice, free of flood exposure (Billings et al., 2022; Wing et al., 2022).

Extending our comparison to the full FEMA zone hierarchy, rather than the 100-year zone alone, would allow a more direct test of whether the same pattern holds in a mountainous, flash-flood-driven event like Helene, rather than Ida's more typical riverine/coastal flooding context.

As Composto et al. (2024) note, comparing a single flood event to FEMA zones, which represent long-term annual flood probability rather than event-specific risk, limits conclusions about the zones' overall effectiveness. The same caveat applies here. Hurricane Helene's rainfall total substantially exceeded historical records for the region, meaning some disagreement with the 100-year flood zone boundary is expected for an event of this magnitude, regardless of mapping accuracy.

Our building-intersection approach with FEMA USA Structures identified 272 structures affected by mapped flooding in Asheville, but this count should be treated as a lower bound on total structural damage. For comparison, county-level damage reports indicate that 1,289 residential and commercial buildings were damaged or destroyed across Buncombe County as of late October 2024 (Callaghan, 2025) — more than four times our satellite-derived count — though this reflects a broader damage-reporting standard (including wind and non-flood damage) across the full county, not flood-specific damage within our more limited Asheville study extent. This is also consistent with journalistic reporting from Asheville's River Arts District, one of the areas hardest hit by Helene's flooding, where up to 80% of buildings were estimated to have sustained damage (Pogrebin and Abrams, 2024), a substantially higher rate than a footprint-intersection approach based solely on mapped surface water would capture in a similarly inundated area. Because our analysis relies solely on flood extent overlapping a building footprint, it cannot capture damage from mechanisms that are not visible from satellites, such as flooded basements, wind damage, or structural failure unrelated to surface inundation. Similarly, structures shielded by tree canopy or cloud cover in the peak-flood imagery would not be flagged as affected even if they were flooded, consistent with the broader flood-extent limitations discussed above. Additionally, because our method flags a structure as affected only when its footprint intersects mapped surface water, buildings adjacent to flooding — for example, those with flooded ground floors or basements from rising groundwater or stormwater backup, without visible surface inundation touching the footprint — would also be missed.

Despite these limitations, rapid satellite-derived structure exposure mapping offers a meaningful advantage over traditional damage assessment methods: it can be produced within hours to days of a flood event, well within the 24-hour to 3-day window emergency response agencies typically need for early decision-making (Hodgson et al., 2009), whereas field-based damage assessments and insurance or federal assistance claims data can take weeks to months to compile. This approach follows a growing body of work that estimates flood exposure by intersecting building footprints with mapped flood extent (e.g., FloodPop, (Gold and Steinberg-McElroy, 2025)), though as with those studies, footprint intersection alone cannot capture the full extent of structural damage. Together, these findings suggest satellite-derived structure exposure mapping is useful for rapid triage, helping responders and planners identify which neighborhoods warrant priority field assessment, even though 272 structures likely undercounts Asheville's true flood-affected building total.

Both nighttime-lights metrics identified Asheville and Buncombe County as the most severely affected areas in the study region, consistent with the scale of damage reported there, including widespread power outages, water infrastructure failure, and extensive flooding of the urban core. This aligns with prior work linking reductions in nighttime radiance to disruption of human activity following natural disasters (Zheng et al., 2025), supporting NTL as a useful proxy for capturing storm impact in and around the region's largest urban center.

However, NTL-based damage assessment has a known limitation that may be particularly relevant to the more rural portions of our study area: NTL is less sensitive to changes in economic activity and infrastructure disruption in rural, non-metro areas, since it primarily detects large-scale lighting changes rather than smaller-scale changes such as individual house lights or small rural businesses (Gibson et al., 2021). Much of our study area outside Asheville is rural and mountainous, with sparser baseline nighttime lighting. In these areas, real disruption to homes, small businesses, and infrastructure may be less likely to register as a detectable change in radiance, even where flood damage occurred. As a result, our NTL-based severity scores may understate disaster impact in the study area's more rural counties relative to Asheville, where denser baseline lighting makes disruptions easier to detect. Ground-truthing NTL-derived damage estimates against another data source in a rural county would help clarify how large this effect is in practice.

Hurricane Helene's landslides and flooding showed that Asheville lacks the protections from climate change and natural hazards that the "climate haven" designation implies, consistent with historical evidence. WNC has experienced significant tropical-cyclone-driven flooding for over a century, including major flood events in 1916, 2004, and now 2024, with an average of one severe flood every nine years between 1924 and 2013 (Amorim et al., 2025). Despite this documented history, flood insurance penetration in the region remains low, with approximately 1.5% of buildings in central and WNC carrying flood insurance in 2024, compared to roughly 14% along the state's coast (Amorim *et al.*, 2025). This reflects a persistent mismatch between perceived and actual flood risk in inland, mountainous areas often assumed to be relatively safe from major storm impacts. Quantifying flood extent and building exposure in a high-population, high-damage area like Asheville can help inform resilience planning and risk communication as the region works to regain its status as a "climate haven," particularly given evidence that the underlying flood risk was neither new nor fully appreciated before Helene struck.

Future work could incorporate SAR data, already applied to Helene via a Sentinel-1-based inundation product (First et al., 2026), and/or expand the time frame to capture long-term recovery. Overall, this study provides a framework for flood mapping and damage assessment that can support emergency response and planning. Extreme weather events are becoming more frequent and intense, and integrating high-resolution satellite imagery with geospatial analysis will be important for improving disaster preparedness and response.

Acknowledgments: This work acknowledges partial research support from a NASA Terrestrial Hydrology Project (Grant Number 80NSSC21K0980, Tulbure PI) for developing the flood maps.

Competing Interests: The authors have no relevant financial or non-financial interests to disclose.

Author Contributions: MGT conceptualized the study, acquired funding, supervised the project, and wrote the final draft. DB performed most analyses and wrote the initial draft. JC, RC, and MDG provided input on analyses and edited the final draft.

References:

Aerts, J.C.J.H., Botzen, W.J.W., Emanuel, K., Lin, N., de Moel, H., Michel-Kerjan, E.O., 2014. Evaluating Flood Resilience Strategies for Coastal Megacities. Science 344, 473–475. https://doi.org/10.1126/science.1248222

Amorim, R., Villarini, G., Czajkowski, J., Smith, J., 2025. Flooding from Hurricane Helene and associated impacts: A historical perspective. J. Hydrol. X 27, 100204. https://doi.org/10.1016/j.hydroa.2025.100204

Anderson, G.B., Schumacher, A., Done, J.M., Hurrell, J.W., 2022. Projecting the Impacts of a Changing Climate: Tropical Cyclones and Flooding. Curr. Environ. Health Rep. 9, 244–262. https://doi.org/10.1007/s40572-022-00340-0

Armon, M., Shmilovitz, Y., Dente, E., 2025. Anatomy of a foreseeable disaster: Lessons from the 2023 dam-breaching flood in Derna, Libya. Sci. Adv. 11, eadu2865. https://doi.org/10.1126/sciadv.adu2865

Aziz, F., Wang, X., Mahmood, M.Q., Awais, M., Trenouth, B., 2024. Coastal urban flood risk management: Challenges and opportunities − A systematic review. J. Hydrol. 645, 132271. https://doi.org/10.1016/j.jhydrol.2024.132271

Balaguru, K., Xu, W., Chang, C.-C., Leung, L.R., Judi, D.R., Hagos, S.M., Wehner, M.F., Kossin, J.P., Ting, M., 2023. Increased U.S. coastal hurricane risk under climate change. Sci. Adv. 9, eadf0259. https://doi.org/10.1126/sciadv.adf0259

Billings, S.B., Gallagher, E.A., Ricketts, L., 2022. Let the rich be flooded: The distribution of financial aid and distress after hurricane harvey. J. Financ. Econ. 146, 797–819. https://doi.org/10.1016/j.jfineco.2021.11.006

Breiman, L., 2001. Random Forests. Mach. Learn. 45, 5–32. https://doi.org/10.1023/A:1010933404324

Callaghan, J., 2025. Disastrous Effects of Hurricane Helene in the Southern Appalachian Mountains Including a Review of Mechanisms Producing Extreme Rainfall. Hydrology 12, 201. https://doi.org/10.3390/hydrology12080201

Chen, A., Giese, M., Chen, D., 2020. Flood impact on Mainland Southeast Asia between 1985 and 2018—The role of tropical cyclones. J. Flood Risk Manag. 13, e12598. https://doi.org/10.1111/jfr3.12598

Cline, M., 2024. Insight Into the Population in Hurricane Helene's Path. URL https://www.osbm.nc.gov/blog/2024/10/07/insight-population-hurricane-helenes-path (accessed 8.27.26).

Collins, E.L., Sanchez, G.M., Terando, A., Stillwell, C.C., Mitasova, H., Sebastian, A., Meentemeyer, R.K., 2022. Predicting flood damage probability across the conterminous United States. Environ. Res. Lett. 17, 034006. https://doi.org/10.1088/1748-9326/ac4f0f

Composto, R.W., Tulbure, M.G., Tiwari, V., Gaines, M.D., Caineta, J., 2024. Quantifying urban flood extent using satellite imagery and machine learning. Nat. Hazards. https://doi.org/10.1007/s11069-024-06817-5

Cooper, R., 2024. Hurricane Helene Recovery. Office of State Budget and Management, Raleigh, NC.

FEMA, 2026. USA Structures.

First, J.M., Sunde, M., Waddle, M., Kintziger, K., Ellis, K., Scales, S., Fazio, J., Houston, J.B., 2026. Flood exposure, health outcomes, and recovery needs following Hurricane Helene in Southern Appalachia. Environ. Hazards 1–26. https://doi.org/10.1080/17477891.2026.2631993

Gaines, M.D., Tulbure, M.G., Perin, V., Composto, R., Tiwari, V., 2024. Projecting Surface Water Area Under Different Climate and Development Scenarios. Earths Future 12, e2024EF004625. https://doi.org/10.1029/2024EF004625

Gibson, J., Olivia, S., Boe-Gibson, G., Li, C., 2021. Which night lights data should we use in economics, and where? J. Dev. Econ. 149, 102602. https://doi.org/10.1016/j.jdeveco.2020.102602

Gold, A.C., Steinberg-McElroy, I., 2025. High-resolution estimates of the US population in fluvial or coastal flood hazard areas. Sci. Data 12, 1377. https://doi.org/10.1038/s41597-025-05717-y

Hagen, A., Cangialosi, J., Chenard, M., Alaka, L., Delgado, S., 2026. National Hurricane Center Tropical Cyclone Report: Hurricane Helene. National Hurricane Center.

Hall, T.M., Kossin, J.P., 2019. Hurricane stalling along the North American coast and implications for rainfall. Npj Clim. Atmos. Sci. 2, 17. https://doi.org/10.1038/s41612-019-0074-8

Hodgson, M.E., Davis, B.A., Kotelenska, J., 2009. Remote Sensing and GIS Data/Information in the Emergency Response/Recovery Phase, in: Showalter, P.S., Lu, Y. (Eds.), Geospatial Techniques in Urban Hazard and Disaster Analysis. Springer Netherlands, Dordrecht, pp. 327–354. https://doi.org/10.1007/978-90-481-2238-7_16

Holland, G., Bruyère, C.L., 2014. Recent intense hurricane response to global climate change. Clim. Dyn. 42, 617–627. https://doi.org/10.1007/s00382-013-1713-0

Hondula, K.L., DeVries, B., Jones, C.N., Palmer, M.A., 2021. Effects of Using High Resolution Satellite-Based Inundation Time Series to Estimate Methane Fluxes From Forested Wetlands. Geophys. Res. Lett. 48. https://doi.org/10.1029/2021GL092556

Jensen, K., De, S., Hughes, L., Yalla, G., 2022. Flood Monitoring with X-Band and C-Band SAR: A Case Study of the 2021 British Columbia Floods, in: IGARSS 2022 - 2022 IEEE International Geoscience and Remote Sensing Symposium. Presented at the IGARSS 2022 - 2022 IEEE International Geoscience and Remote Sensing Symposium, pp. 5535–5538. https://doi.org/10.1109/IGARSS46834.2022.9884604

Khan, A., Chadwick, A.E., Daniels, N.K., Dabelko, G.D., Krometis, L.-A., Shinn, J.E., Lynch, A.J., Garner, E., Hession, W.C., Bowman, J., 2025. Extreme Weather Events and Risk Communication Challenges in Central Appalachia: A Qualitative Inquiry. J. Contingencies Crisis Manag. 33, e70057. https://doi.org/10.1111/1468-5973.70057

Knutson, T., Camargo, S.J., Chan, J.C.L., Emanuel, K., Ho, C.-H., Kossin, J., Mohapatra, M., Satoh, M., Sugi, M., Walsh, K., Wu, L., 2020. Tropical Cyclones and Climate Change Assessment: Part II: Projected Response to Anthropogenic Warming. Bull. Am. Meteorol. Soc. 101, E303–E322. https://doi.org/10.1175/BAMS-D-18-0194.1

Kriegler, F.J., Malila, W.A., Nalepka, R.F., Richardson, W., 1969. Preprocessing Transformations and Their Effects on Multispectral Recognition. Presented at the Remote Sensing of Environment, VI.

Landwehr, T., Dasgupta, A., Waske, B., 2024. Towards robust validation strategies for EO flood maps. Remote Sens. Environ. 315, 114439. https://doi.org/10.1016/j.rse.2024.114439
Langhorst, T., Andreadis, K.M., Allen, G.H., 2024. Global Cloud Biases in Optical Satellite Remote Sensing of Rivers. Geophys. Res. Lett. 51, e2024GL110085. https://doi.org/10.1029/2024GL110085
Levin, N., Phinn, S., 2022. Assessing the 2022 Flood Impacts in Queensland Combining Daytime and Nighttime Optical and Imaging Radar Data. Remote Sens. 14, 5009. https://doi.org/10.3390/rs14195009
Maxwell, A.E., Warner, T.A., Fang, F., 2018. Implementation of machine-learning classification in remote sensing: an applied review. Int. J. Remote Sens. 39, 2784–2817. https://doi.org/10.1080/01431161.2018.1433343
McCabe, M.F., Aragon, B., Houborg, R., Mascaro, J., 2017. CubeSats in Hydrology: Ultrahigh-Resolution Insights Into Vegetation Dynamics and Terrestrial Evaporation. Water Resour. Res. 53, 10017–10024. https://doi.org/10.1002/2017WR022240
McFeeters, S.K., 1996. The use of the Normalized Difference Water Index (NDWI) in the delineation of open water features. Int. J. Remote Sens. 17, 1425–1432. https://doi.org/10.1080/01431169608948714
Mullen, A.L., Watts, J.D., Rogers, B.M., Carroll, M.L., Elder, C.D., Noomah, J., Williams, Z., Caraballo-Vega, J.A., Bredder, A., Rickenbaugh, E., Levenson, E., Cooley, S.W., Hung, J.K.Y., Fiske, G., Potter, S., Yang, Y., Miller, C.E., Natali, S.M., Douglas, T.A., Kyzivat, E.D., 2023. Using High-Resolution Satellite Imagery and Deep Learning to Track Dynamic Seasonality in Small Water Bodies. Geophys. Res. Lett. 50, e2022GL102327. https://doi.org/10.1029/2022GL102327
Munawar, H.S., Hammad, A.W.A., Waller, S.T., 2022. Remote Sensing Methods for Flood Prediction: A Review. Sensors 22, 960. https://doi.org/10.3390/s22030960
National Geodetic Survey, 2024. Hurricane Helene Damage Assessment Imagery [WWW Document]. URL https://oceanservice.noaa.gov/news/sep24/ngs-storm-imagery-helene.html
NOAA National Severe Storms Laboratory, 2024. Flood Basics [WWW Document]. Sev. Weather 101. URL https://www.nssl.noaa.gov/education/svrwx101/floods/
Noh, S., Lee, J.-H., Lee, S., Seo, D.-J., 2019. Retrospective Dynamic Inundation Mapping of Hurricane Harvey Flooding in the Houston Metropolitan Area Using High-Resolution Modeling and High-Performance Computing. Water 11, 597. https://doi.org/10.3390/w11030597
Pastor-Escuredo, D., Torres, Y., Martínez-Torres, M., Zufiria, P.J., 2020. Rapid Multi-Dimensional Impact Assessment of Floods. Sustainability 12, 4246. https://doi.org/10.3390/su12104246
Patricola, C.M., Wehner, M.F., 2018. Anthropogenic influences on major tropical cyclone events. Nature 563, 339–346. https://doi.org/10.1038/s41586-018-0673-2
Pedregosa, F., Varoquaux, G., Gramfort, A., Michel, V., Thirion, B., Grisel, O., Blondel, M., Prettenhofer, P., Weiss, R., Dubourg, V., Vanderplas, J., Passos, A., Cournapeau, D., Brucher, M., Perrot, M., Duchesnay, É., 2011. Scikit-learn: Machine Learning in Python. J Mach Learn Res 12, 2825–2830.

673 Perin, V., Tulbure, M.G., Gaines, M.D., Reba, M.L., Yaeger, M.A., 2022. A multi-sensor satellite
674 imagery approach to monitor on-farm reservoirs. Remote Sens. Environ. 270, 112796.
675 https://doi.org/10.1016/j.rse.2021.112796
676 Phan, T.N., Kuch, V., Lehnert, L.W., 2020. Land Cover Classification using Google Earth
677 Engine and Random Forest Classifier—The Role of Image Composition. Remote Sens.
678 12, 2411. https://doi.org/10.3390/rs12152411
679 Pieper, K.J., Beighley, E., Jones, C.N., Drewry, K., Jamshidi, R., Li, Y., Michael, L., Mize, W.,
680 Fowlkes, J., Blethen, A., Wang, Q.R., Bailey, E., Kane, M., Goforth, C., Kane, E.,
681 McCaully, R., King, C., Webb, A., Goggins, B., Duvvuri, B., Bartuska, E., Tang, T., Li,
682 W., 2025. Responding after Hurricane Helene: Rapidly Estimating Impacts to
683 Environmental Health Services in North Carolina. Environ. Sci. Technol. Lett. 12, 820–
684 826. https://doi.org/10.1021/acs.estlett.5c00503
685 Planet Labs, 2026. PlanetScope.
686 Pogrebin, R., Abrams, J., 2024. Arts District, Decades in the Making, in Ruins After Helene. N.
687 Y. Times.
688 Rappaport, E.N., 2014. Fatalities in the United States from Atlantic Tropical Cyclones: New Data
689 and Interpretation. Bull. Am. Meteorol. Soc. 95, 341–346. https://doi.org/10.1175/BAMS-
690 D-12-00074.1
691 Risser, M.D., Wehner, M.F., 2017. Attributable Human-Induced Changes in the Likelihood and
692 Magnitude of the Observed Extreme Precipitation during Hurricane Harvey. Geophys.
693 Res. Lett. 44. https://doi.org/10.1002/2017GL075888
694 Salarieh, B., Ugwu, I.A., Salman, A.M., 2023. Impact of changes in sea surface temperature due
695 to climate change on hurricane wind and storm surge hazards across US Atlantic and
696 Gulf coast regions. SN Appl. Sci. 5, 205. https://doi.org/10.1007/s42452-023-05423-7
697 Shao, Z., Li, X., 2023. Multi-scale estimation of poverty rate using night-time light imagery. Int. J.
698 Appl. Earth Obs. Geoinformation 121, 103375.
699 https://doi.org/10.1016/j.jag.2023.103375
700 Shastry, A., Carter, E., Coltin, B., Sleeter, R., McMichael, S., Eggleston, J., 2023. Mapping
701 floods from remote sensing data and quantifying the effects of surface obstruction by
702 clouds and vegetation. Remote Sens. Environ. 291, 113556.
703 https://doi.org/10.1016/j.rse.2023.113556
704 Simon, J., 2024. They came to Asheville looking for a “climate haven.” Then came Hurricane
705 Helene. NPR.
706 Su, S., Tian, J., Dong, X., Tian, Q., Wang, N., Xi, Y., 2022. An Impervious Surface Spectral
707 Index on Multispectral Imagery Using Visible and Near-Infrared Bands. Remote Sens.
708 14, 3391. https://doi.org/10.3390/rs14143391
709 Tan, W., Qin, N., Zhang, Y., McGrath, H., Fortin, M., Li, J., 2024. A rapid high-resolution multi-
710 sensory urban flood mapping framework via DEM upscaling. Remote Sens. Environ.
711 301, 113956. https://doi.org/10.1016/j.rse.2023.113956
712 Tulbure, M.G., Broich, M., Perin, V., Gaines, M., Ju, J., Stehman, S.V., Pavelsky, T., Masek,
713 J.G., Yin, S., Mai, J., Betbeder-Matibet, L., 2022. Can we detect more ephemeral floods
714 with higher density harmonized Landsat Sentinel 2 data compared to Landsat 8 alone?
715 ISPRS J. Photogramm. Remote Sens. 185, 232–246.
716 https://doi.org/10.1016/j.isprsjprs.2022.01.021

Tulbure, M.G., Broich, M., Stehman, S.V., Kommareddy, A., 2016. Surface water extent dynamics from three decades of seasonally continuous Landsat time series at subcontinental scale in a semi-arid region. Remote Sens. Environ. 178, 142–157. https://doi.org/10.1016/j.rse.2016.02.034

United States Congress Joint Economic Committee, Democratic Staff, 2024. Flooding Costs the U.S. Between $179.8 and $496.0 Billion Each Year. U.S. Congress Joint Economic Committee.

U.S. Census Bureau, 2020. ZIP Code Tabulation Areas.

Vicente, G., Marty, R., 2024. worldbank/blackmarblepy: v2024.08.1. https://doi.org/10.5281/ZENODO.10667907

Wang, Z., 2022. Black Marble User Guide (Collection 2.0).

Wang, Z., Vivoni, E.R., 2022. Mapping Flash Flood Hazards in Arid Regions Using CubeSats. Remote Sens. 14, 4218. https://doi.org/10.3390/rs14174218

Wing, O.E.J., Bates, P.D., Smith, A.M., Sampson, C.C., Johnson, K.A., Fargione, J., Morefield, P., 2018. Estimates of present and future flood risk in the conterminous United States. Environ. Res. Lett. 13, 034023. https://doi.org/10.1088/1748-9326/aaac65

Wing, O.E.J., Lehman, W., Bates, P.D., Sampson, C.C., Quinn, N., Smith, A.M., Neal, J.C., Porter, J.R., Kousky, C., 2022. Inequitable patterns of US flood risk in the Anthropocene. Nat. Clim. Change 12, 156–162. https://doi.org/10.1038/s41558-021-01265-6

World Meteorological Organization (WMO), 2023. State of Climate in Asia 2022 (No. WMO-No. 1321). Geneva.

Xia, J., Falconer, R.A., Lin, B., Tan, G., 2011. Numerical assessment of flood hazard risk to people and vehicles in flash floods. Environ. Model. Softw. 26, 987–998. https://doi.org/10.1016/j.envsoft.2011.02.017

Xu, J., Qiang, Y., 2021. Spatial Assessment of Community Resilience from 2012 Hurricane Sandy Using Nighttime Light. Remote Sens. 13, 4128. https://doi.org/10.3390/rs13204128

Zhang, W., Villarini, G., Vecchi, G.A., Smith, J.A., 2018. Urbanization exacerbated the rainfall and flooding caused by hurricane Harvey in Houston. Nature 563, 384–388. https://doi.org/10.1038/s41586-018-0676-z

Zheng, Q., Zeng, Y., Zhou, Y., Wang, Z., Mu, T., Weng, Q., 2025. Nighttime lights reveal substantial spatial heterogeneity and inequality in post-hurricane recovery. Remote Sens. Environ. 319, 114645. https://doi.org/10.1016/j.rse.2025.114645

Zhu, L., Quiring, S.M., 2022. Exposure to precipitation from tropical cyclones has increased over the continental United States from 1948 to 2019. Commun. Earth Environ. 3, 312. https://doi.org/10.1038/s43247-022-00639-8